DQ-Frame Zero-Crossing Effect Modeling and Current Distortion Compensation Method for Vienna Rectifier

Zheyu Miao, *Student Member, IEEE*, Hao Tong, Xiaoguang Jin, Wenxi Yao, *Member, IEEE*, Zhengyu Lu, *Senior Member, IEEE*, and Zhen Ma

***Abstract*—Vienna rectifiers are widely used as front-end rectifiers in many applications because of their high efficiency and high power density. However, this topology has a problem that its current is always distorted near zero-crossing points, especially when the converter-side current ripples are large. This article reveals and models the zero-crossing current distortion phenomenon, which is caused by nonshared vectors of adjacent sectors when the sector detection error occurs. Near the zero-crossing points, the inevitably sector detection errors will occur due to the presence of the switching current ripples and other factors such as the control delay. The errors can be divided into two types, namely, the lag error, and the lead error. The effects of the two types of errors are equivalently modeled in the *dq* frame in this article. When the detection error occurs, it is equivalent to applying additional interference terms to the control output. Based on the equivalent error model, this article proposes two compensation methods to eliminate the zero-crossing effect caused by the sector error. The proposed methods are effective and easy-to-implement. Finally, simulation and experimental results validate the theoretical analysis.**

***Index Terms*—Nonshared vector, sector detection error, Vienna rectifier, zero-crossing current distortion.**

I. Introduction

THE Vienna rectifier is one of the most popular topologies in telecommunication power systems, wind turbine systems and power factor correction systems because of its good performance [1]–[5]. The carried-based pulsewidth modulation (CBPWM) and the space vector pulsewidth modulation (SVPWM) are two basic modulation methods for the Vienna rectifier. Nevertheless, the two kinds of methods can be proved equivalent in essential [6], [7].

Many CBPWM methods are researched and proposed for convenience of implementation [8]–[11]. The classical CBPWM methods use the current or voltage phase to choose the switching signals. The researchers proposed control strategies based on CBPWM to improve its performance, such as balancing the neutral-point voltage [11], realizing variable power factor [8], or adapting undesirable grid conditions [9]. Similarly, SVPWM methods are also widely studied [6], [7], [12]. The SVPWM methods are more flexible and can be configured to realize different performance properties [12]. For example, the Vienna rectifier with variable power factor can be achieved by SVPWM methods considering the sign of currents [7], [8]; the neutral-point voltage can be balanced by adjusting the small vectors in the SVPWM [11]. For the Vienna rectifier, only eight vectors are feasible for every 60° (every sector). Moreover, a switching state may correspond to different voltage vectors in different sectors. Generally, no matter which switching strategy is used, the direction of current is detected to determine the switching state [13]. This is because when the current direction is different, the converter input voltage is different even with the same switching state.

The input current quality is an important indicator of Vienna rectifiers [14], [15]. Due to the switching ripple in the converter-side current, however, the detection of the current direction can never be completely correct near the zero crossings. The zero-crossing distortion problem becomes more serious when the converter-side current ripples are large (for example, an *LCL* filter is used instead of an *LC* filter). In [16], distortions in the vicinity of zero crossings can be observed in the final experimental results and the authors explain the existence of this phenomenon. In fact, due to the existence of nonshared vectors of adjacent sectors, the actual input voltage vector is different from the expectation when lag error or lead error occurs. Some literatures proposed methods considering this issue [16]–[19], [22], but few articles clearly model this problem from the perspective of the system loop. In [17], the switches near the current zero-crossing point are kept "ON" to eliminate the distortion caused by the detection error. Unfortunately, when the switches are kept "ON" state, only two-phase switches work. The control of the switch that does not operate is lost and the ripple will increase. It is still a distortion near the zero crossings, especially when the inductance is small. An improved SVPWM scheme for Vienna rectifiers without current distortion is the proposed without using the nonshared vectors of adjacent sectors [18]. However, five-segment SVPWM is used in this case. The input current ripples and the midpoint voltage fluctuation become

Manuscript received March 21, 2019; revised September 13, 2019; accepted November 27, 2019. Date of publication December 2, 2019; date of current version March 13, 2020. This work was supported by the National Natural Science Foundation of China under Grant 51677168. Recommended for publication by Associate Editor T. Shimizu. *(Corresponding author: Wenxi Yao.)*

Z. Miao, H. Tong, X. Jin, W. Yao, and Z. Lu are with the College of Electrical Engineering, Zhejiang University, Zhejiang 310027, China (e-mail: predatory@zju.edu.cn; 21810065@zju.edu.cn; jxg@zju.edu.cn; ywxi@zju.edu.cn; eeluzy@cee.zju.edu.cn).

Z. Ma is with the Shanghai Institute of Space Power-Sources, Shanghai 200245, China (e-mail: mazhen810615@126.com).

Color versions of one or more of the figures in this article are available online at http://ieeexplore.ieee.org.

Digital Object Identifier 10.1109/TPEL.2019.2957540

larger. The cause of zero-crossing distortion is analyzed by P-type and N-type small vectors in [20]. A zero-sequence component injection modulation method is proposed considering the unbalance dc-link voltage based on CBPWM. Discontinuous PWM methods are not as sensitive as the continuous PWM methods on the issue of zero-crossing distortion. A carrier-based discontinuous PWM method with a variable power factor is proposed in [8] and a discontinuous SVPWM method is presented in [21]. However, discontinuous PWM methods usually cause larger current ripples and harmonics on the converter side. The costs of filters and devices tend to be higher.

To solve the zero-crossing distortion problem for Vienna converters, especially for those using small converter-side inductance (*LCL*/*LLCL*) with high bandwidth current controller, this article models the distortion phenomenon in the *dq* frame and proposes compensation methods. According to the impact, the sector detection errors are divided into two types: lag error, and lead error. The lag error means that the detected sector lags behind the actual sector. On the contrary, the lead error means that the detected sector leads the actual sector. When the sector detection error occurs, the nonshared switching states will cause vector error. The zero-crossing effect is equivalent to applying additional interference terms to the control output. By compensating the interference terms, the zero-crossing distortion can be reduced greatly. Two easy-to-implement and effective controller-based compensation methods, rather than a modulation-based approach, are proposed based on the model for traditional SVPWM and CBPWM.

The article is organized as follows. The concept and impact of the nonshared vectors is presented Section II. When the sector error occurs, the interference terms are added to the loop due to the presence of the nonshared vectors. Section III analyzes and models the influence of the sector detection error. By converting the interference terms into the *dq* coordinate system, the effect of the inevitable sector error near the zero-crossing points is much clearer. Based on the equivalent error model, the compensation methods are proposed in Section IV to reduce or eliminate the adverse effects caused by the sector error. In order to better demonstrate the analysis, the simulations are accompanied in this section. In Section V, the experimental results are presented and discussed. Moreover, the proposed method is compared with the existing ones. Finally, the main points of this article are summarized in Section VI.

II. Nonshared Vectors of Vienna Rectifier and Their Influence

Fig. 1 shows the typical topology and control scheme of Vienna rectifiers. The bidirectional switch is consisted by two series MOSFETs with a connected source pin [2], which is shown at the bottom of Fig. 1(a). The rectifier input phase voltage v_{si} $(i = a, b, c)$ is determined by the switching states S_i and the direction of the corresponding converter-side current i_{si}. $S_i = 1$ means the switch is on; $S_i = 0$ means the switch is off. The output dc voltage u_o is usually controlled as a constant V_o and the neutral-point voltage u_m is controlled to keep balance

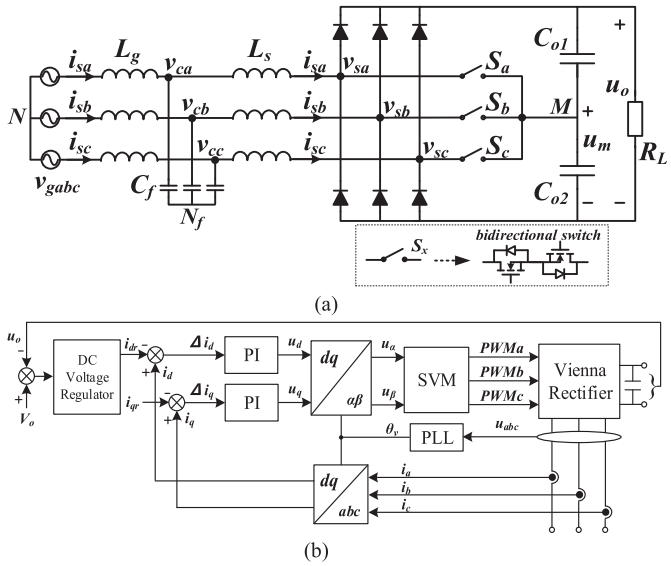

Fig. 1. Topology and control scheme of Vienna rectifiers. (a) Topology. (b) Control scheme.

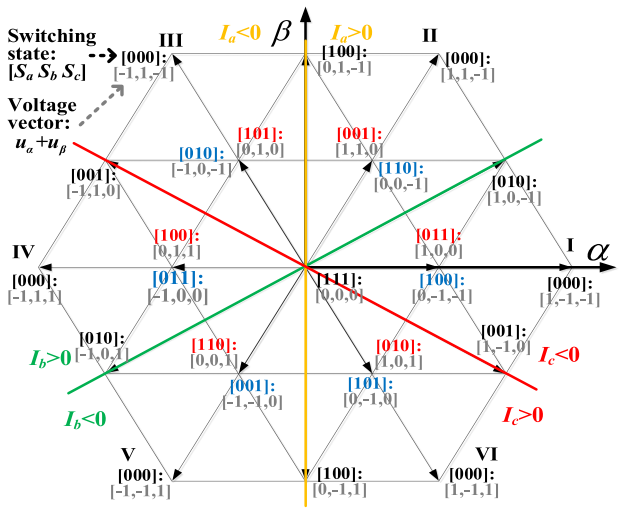

Fig. 2. Switching states and voltage vectors of Vienna rectifiers.

$(u_m = 1/2u_o)$. Fig. 2 shows the achievable voltage vectors in each sector and the corresponding switching states $[S_a, S_b, S_c]$.

The cause of zero-crossing distortion is analyzed by the small vectors [20], since one switching state can correspond to different small voltage vectors in different sectors. For example, the switching state [001] corresponds to the voltage vector [1,−1,0] in sector I, but it corresponds to the voltage vector [1,1,0] in sector II. These small vectors can be further divided and analyzed in detail in each sector. In this article, the nonshared vectors of adjacent sectors are defined as the different voltage vectors corresponding to one identical switching state, where a pair of nonshared vectors are always near the boundary of the two sectors; the corresponding switching state is called the nonshared switching state. To better illustrate this definition, Fig. 3 gives the nonshared vectors of sectors I and II as an example. When

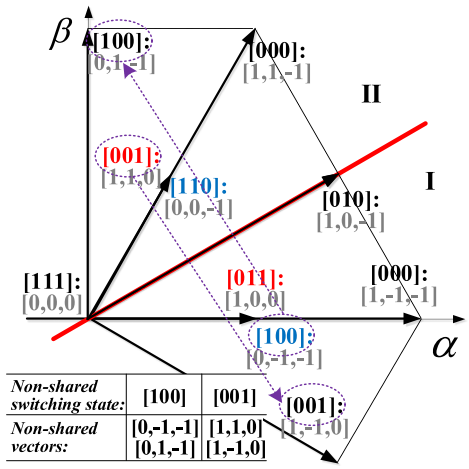

Fig. 3. Nonshared vectors for sectors I and II.

sector detection error occurs, there are two possible cases: one case is the lag error, in which the detected sector lags behind the actual sector; the other case is the lead error, in which the detected sector leads the actual sector. When lag error occurs, the actual vector will lead the expected vector due to the existence of nonshared switching states. On the contrary, when lead error occurs, the actual vector will lag behind the expected vector. In both cases, the real voltage vector is different from expectation and the zero-crossing effect occurs.

Let the output of the controller in the dq domain be (u_d, u_q), and the corresponding control reference in the $\alpha\beta$ frame is $(u_{\alpha 0}, u_{\beta 0})$. The phase angle used in the synchronous coordinate system is θ_v, which is usually obtained by the phase-locked loop. Then, there is

$$\begin{bmatrix} u_{\alpha 0} \\ u_{\beta 0} \end{bmatrix} = \begin{bmatrix} \cos\theta_v & -\sin\theta_v \\ \sin\theta_v & \cos\theta_v \end{bmatrix} \begin{bmatrix} u_d \\ u_q \end{bmatrix} = \mathbf{T}_{dq/\alpha\beta} \begin{bmatrix} u_d \\ u_q \end{bmatrix}. \quad (1)$$

If the lag error occurs near the boundary of sectors I and II, the detected sector in this control period is the sector I and the actual sector is sector II. This case is shown in Fig. 4(a). The expected control output $(u_{\alpha 0}, u_{\beta 0})$ is in the triangular sub-sector surrounded by the switching states [010], [110], and [011/100]. The switching states [010], [110], and [011/100] correspond to the voltage vector [1, 0, −1], [0, 0, −1], and [1, 0, 0/0, −1, −1], respectively. Since the detected sector is sector I, the switching state [001] is not used. At this point, the switching state [100] is the nonshared switching state; the voltage vectors [0, 1, −1] and [0, −1, −1] are a pair of nonshared vectors. According to the vector synthesis rules, the action time of each switching state can be calculated from

$$\begin{cases} t_1 + t_2 + t_3 = T_s \\ \frac{\sqrt{3}}{6} V_o (t_1 + t_2) = u_{\beta 0} T_s \\ \frac{V_o}{2} t_1 + \frac{V_o}{6} t_2 + \frac{V_o}{3} t_3 = u_{\alpha 0} T_s \end{cases} \quad (2)$$

where t_1 is the action time of switching state [010]; t_1 is the action time of switching state [110]; and t_3 is the total action time of vector switching states [011/100].

After solving the above formula, there is

$$\begin{cases} \frac{t_1}{T_s} = \frac{3u_{\alpha 0}}{V_o} + \frac{\sqrt{3}u_{\beta 0}}{V_o} - 1 \\ \frac{t_2}{T_s} = -\frac{3u_{\alpha 0}}{V_o} + \frac{\sqrt{3}u_{\beta 0}}{V_o} + 1 \\ \frac{t_3}{T_s} = 1 - \frac{2\sqrt{3}u_{\beta 0}}{V_o}. \end{cases} \quad (3)$$

If the total output current of neutral point is 0, the switching states [011] and [100] both have a duration of $t_3/2$. Since the actual sector is sector II and the nonshared switching state [100] is used, the actual input voltage $(u_{\alpha 1}, u_{\beta 1})$ is calculated as

$$\begin{aligned} (u_{\alpha 1}, u_{\beta 1}) &= \frac{t_1}{T_s}\overrightarrow{v_1} + \frac{t_2}{T_s}\overrightarrow{v_2} + \frac{t_3}{2T_s}\left(\overrightarrow{v_3} + \overrightarrow{v_3'}\right) \\ &= \left(u_{\alpha 0} + \frac{2\sqrt{3}u_{\beta 0} - V_o}{6}, \frac{\sqrt{3}V_o}{6}\right) \end{aligned} \quad (4)$$

where v_1 is the voltage vector [1, 0, −1]; v_2 is the voltage vector [0, 0, −1]; v_3 is the voltage vector [1, 0, 0]; and v_3' is the voltage vector [0, 1, −1], which is the nonshared vector of [0, −1, −1].

Similarly, when the lead error occurs near the boundary of sectors I and II, the detected sector is the sector II and the actual sector is sector I. This case is shown in Fig. 4(b). The switching state [001] is the nonshared switching state; the voltage vectors [1, 1, 0] and [1, −1, 0] are a pair of nonshared vectors. In this case, the actual input voltage $(u_{\alpha 1}, u_{\beta 1})$ is

$$(u_{\alpha 1}, u_{\beta 1}) = \left(\frac{u_{\alpha 0}}{2} + \frac{\sqrt{3}u_{\beta 0}}{6} + \frac{V_o}{6}, \frac{\sqrt{3}u_{\alpha 0}}{2} + \frac{u_{\beta 0}}{2} - \frac{\sqrt{3}V_o}{6}\right). \quad (5)$$

Table I summarizes all the nonshared switching states and vectors for each sector boundary. By analyzing all sectors, it can be found that all the nonshared vectors of adjacent sectors have the same relationship. The analysis of other sectors can be equivalent to the analysis of sectors I and II. Therefore, there are unified conclusions for all sectors as follows.

1) Due to the presence of the nonshared switching states, the actual input voltage vector is different from the expected control value. The actual vector and the expected vector constitute a pair of nonshared vectors.
2) For a pair of nonshared vectors, the actual vectors are obtained by rotating the expected vectors 90° counter-clockwise and then multiplying it by $\sqrt{3}$ when the lag error occurs. The actual vectors are obtained by rotating the expected vectors 90° clockwise and then multiplying it by $\sqrt{3}$ when the lead error occurs. This is mathematically expressed as

$$\overrightarrow{v_{\text{at}}} = \begin{cases} \sqrt{3}\begin{bmatrix} \cos 90^\circ & -\sin 90^\circ \\ \sin 90^\circ & \cos 90^\circ \end{bmatrix} \overrightarrow{v_{ex}}, & \text{Lag error} \\ \sqrt{3}\begin{bmatrix} \cos 90^\circ & \sin 90^\circ \\ -\sin 90^\circ & \cos 90^\circ \end{bmatrix} \overrightarrow{v_{ex}}, & \text{Lead error} \end{cases} \quad (6)$$

where $\overrightarrow{v_{\text{at}}}$ is the actual voltage vector for a nonshared switching state; and $\overrightarrow{v_{\text{ex}}}$ is the expected voltage vector for the same nonshared switching state. From (6), the actual voltage vector will lead the expected vector when the lag error occurs. On the

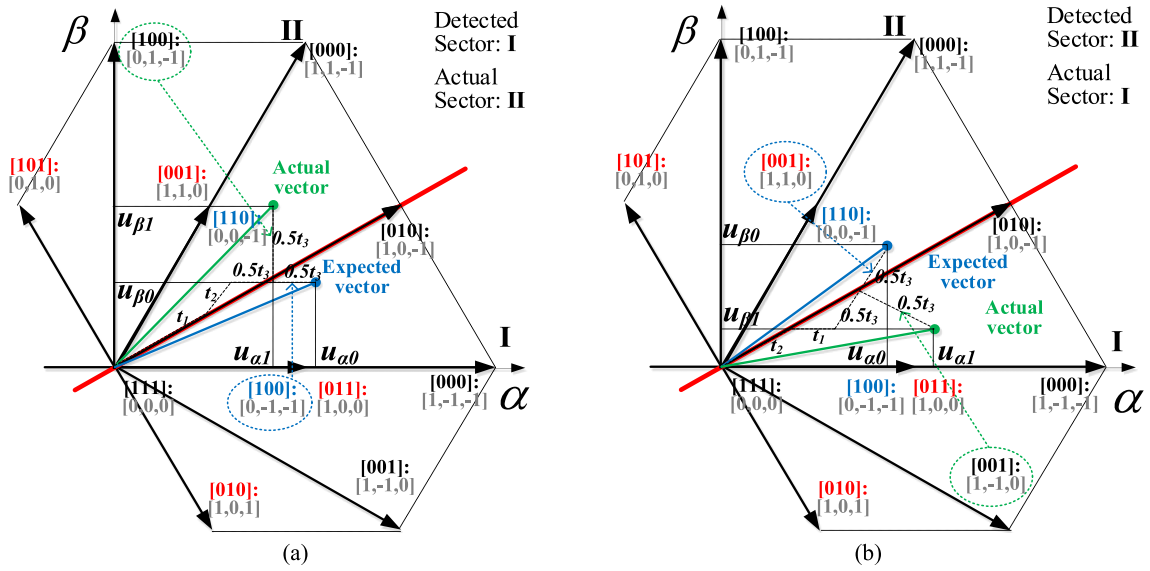

Fig. 4. Effect of nonshared vectors when the sector detection error occurs. (a) Lag error occurs. (b) Lead error occurs.

TABLE I
NONSHARED SWITCHING STATES AND VECTORS

Lag error			Lead error		
Non-shared switching state	Actual sector/ Detected sector	Actual vector/ Expected vector	Non-shared switching state	Actual sector/ Detected sector	Actual vector/ Expected vector
[100]	II / I	[0,1,-1]/ [0,-1,-1]	[001]	I / II	[1,-1,0]/ [1,1,0]
[001]	III / II	[-1,1,0]/[1,1,0]	[010]	II / III	[1,0,-1]/ [-1,0,-1]
[010]	IV / III	[-1,0,1]/[-1,0,-1]	[100]	III / IV	[0,1,-1]/ [0,1,1]
[100]	V / IV	[0,-1,1]/[0,1,1]	[001]	IV / V	[-1,1,0]/ [-1,-1,0]
[001]	VI / V	[1,-1,0]/[-1,-1,0]	[010]	V / VI	[-1,0,1]/ [1,0,1]
[010]	V / I	[1,0,-1]/[1,0,1]	[100]	VI / I	[0,-1,1]/ [0,-1,-1]

contrary, when the lead error occurs, the actual voltage vector will lag behind the expected vector.

3) Whether using CBPWM methods or SVPWM methods, the use of nonshared switching states will inevitably result in the emergence of nonshared voltage vectors.

III. PROPOSED MODEL FOR ZERO-CROSSING EFFECT

In a digital control system, the sampled current is generally smooth and the switching ripples are avoided. However, there are switching ripples in the actual converter-side input current, so the sector in which the converter is located is actually constantly switching near the zero-crossing points. Whether the detected sector is judged by the line voltage or the input current, the actual sector will switch due to the current switching. The total phase delay t_{del} (sampling delay for the current-based judgment / phase shift for the voltage-based judgment) will further affect the correct rate of sector detection. Fig. 5 shows the schematic diagram of the sampled current and the actual converter-side current. The actual and the detected sector numbers are also shown according to the actual and the sampled current. In the case of unit power factor, the positions of the current vector and the voltage vector are basically the same. As shown in Fig. 5, the lag error always

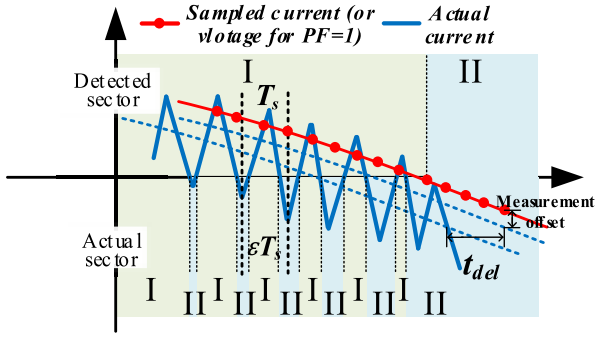

Fig. 5. Actual current, sampled current and corresponding sectors.

occurs before the determination of sector switching, while the lead error usually occurs after the switching. Unfortunately, due to current ripples, sampling delay and measurement offset, the sector detection error is unavoidable. Near zero crossings, the sector is correct for only part of a cycle and the zero-crossing effect occurs.

In one switching period, the accuracy of the sector detection is ε, which is shown in Fig. 5. Therefore, the actual voltage output

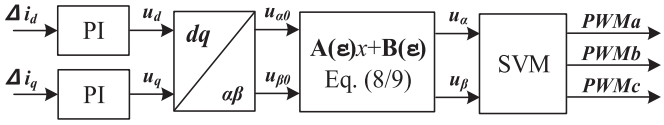

Fig. 6. Equivalent control block considering the zero-crossing effect.

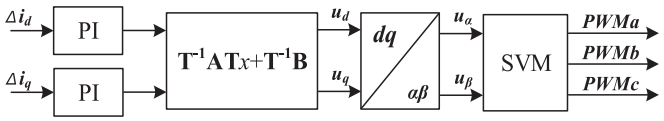

Fig. 7. Equivalent control block considering zero-crossing effect in *dq* frame.

of a switching cycle is expressed as

$$(u_\alpha, u_\beta) = \varepsilon\,(u_{\alpha 0}, u_{\beta 0}) + (1-\varepsilon)\,(u_{\alpha 1}, u_{\beta 1})\,. \tag{7}$$

When the lag error occurs, there is

$$\begin{bmatrix} u_\alpha \\ u_\beta \end{bmatrix} = \begin{bmatrix} 1 & \frac{\varepsilon'}{\sqrt{3}} \\ 0 & \varepsilon \end{bmatrix} \begin{bmatrix} u_{\alpha 0} \\ u_{\beta 0} \end{bmatrix} + \begin{bmatrix} \frac{-\varepsilon' V_o}{6} \\ \frac{\varepsilon' V_o}{2\sqrt{3}} \end{bmatrix} \tag{8}$$

where $\varepsilon' = 1-\varepsilon$.

Similarly, when the lead error occurs, there is

$$\begin{bmatrix} u_\alpha \\ u_\beta \end{bmatrix} = \begin{bmatrix} \frac{1+\varepsilon}{2} & \frac{\varepsilon'}{2\sqrt{3}} \\ \frac{\varepsilon'\sqrt{3}}{2} & \frac{1+\varepsilon}{2} \end{bmatrix} \begin{bmatrix} u_{\alpha 0} \\ u_{\beta 0} \end{bmatrix} + \begin{bmatrix} \frac{\varepsilon' V_o}{6} \\ \frac{-\varepsilon' V_o}{2\sqrt{3}} \end{bmatrix}. \tag{9}$$

After considering the zero-crossing effect, the actual equivalent control block is shown in Fig. 6. To better reflect the zero-crossing effect, the above expressions characterizing the zero-crossing effect are transformed into the *dq* coordinate system (10), which is shown in Fig. 7

$$\begin{aligned} \begin{bmatrix} u_\alpha \\ u_\beta \end{bmatrix} &= \mathbf{A}\,(\varepsilon)\,\mathbf{T}_{dq/\alpha\beta} \begin{bmatrix} u_d \\ u_q \end{bmatrix} + \mathbf{B}\,(\varepsilon) \\ &= \mathbf{T}_{dq/\alpha\beta} \left(\mathbf{T}^{-1}_{dq/\alpha\beta} \mathbf{A} \mathbf{T}_{dq/\alpha\beta} \begin{bmatrix} u_d \\ u_q \end{bmatrix} \right) \\ &\quad + \mathbf{T}_{dq/\alpha\beta} \left(\mathbf{T}^{-1}_{dq/\alpha\beta} \mathbf{B} \right) \end{aligned} \tag{10}$$

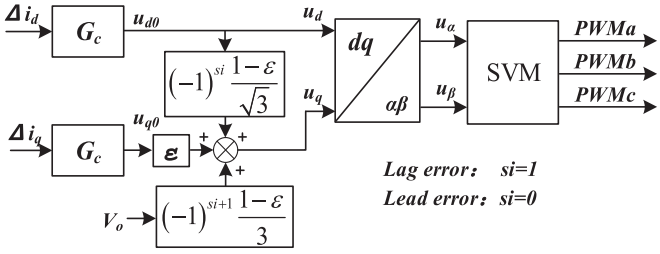

Fig. 8. Equivalent model considering zero-crossing effect under unity power factor.

where

$$\mathbf{T}_{dq/\alpha\beta} = \begin{bmatrix} \cos\theta_v & -\sin\theta_v \\ \sin\theta_v & \cos\theta_v \end{bmatrix}; \mathbf{T}^{-1}_{dq/\alpha\beta} = \begin{bmatrix} \cos\theta_v & \sin\theta_v \\ -\sin\theta_v & \cos\theta_v \end{bmatrix}.$$

When the lag error occurs, the corresponding matrices describe the zero-crossing effect are derived as (11). Similarly, when the lead error occurs, the matrices are derived as (12). These matrices are shown at the bottom of the page.

Because the zero-crossing effect occurs in a small range near the current zero-crossing points, θ_v changes little and the phase value at the zero-crossing time can be substituted into the above formula. Taking the unity power factor as an example, there is $\theta_v = \pi/6$. In this case, the aforementioned matrices used to describe the zero-crossing effect are derived as

$$\mathbf{T}^{-1}_{dq/\alpha\beta} \mathbf{A} \mathbf{T}_{dq/\alpha\beta} = \begin{bmatrix} 1 & 0 \\ (-1)^{si} \frac{1-\varepsilon}{\sqrt{3}} & \varepsilon \end{bmatrix} \tag{13}$$

$$\mathbf{T}^{-1}_{dq/\alpha\beta} \mathbf{B} = \begin{bmatrix} 0 \\ (-1)^{si+1} \frac{(1-\varepsilon)V_o}{3} \end{bmatrix} \tag{14}$$

where $si = 1$ if the lag error occurs; and $si = 0$ if the lead error occurs.

Therefore, the *dq*-frame equivalent model considering the zero-point effect is shown in Fig. 8. From the proposed model in Fig. 8, the cause and process of the current distortion problem at zero-crossing points are much clearer and quantified. In the case that the Vienna rectifier works with the unity power factor,

$$\text{Lag error}: \begin{cases} \mathbf{T}^{-1}_{dq/\alpha\beta} \mathbf{A} \mathbf{T}_{dq/\alpha\beta} = \begin{bmatrix} 1-\varepsilon' \sin\theta_v{}^2 + \frac{\varepsilon'}{\sqrt{3}} \sin\theta_v \cos\theta_v & -\varepsilon' \sin\theta_v \cos\theta_v + \frac{\varepsilon'}{\sqrt{3}} \cos\theta_v{}^2 \\ -\varepsilon' \sin\theta_v \cos\theta_v - \frac{\varepsilon'}{\sqrt{3}} \sin\theta_v{}^2 & 1-\varepsilon' \cos\theta_v{}^2 - \frac{\varepsilon'}{\sqrt{3}} \sin\theta_v \cos\theta_v \end{bmatrix} \\ \mathbf{T}^{-1}_{dq/\alpha\beta} \mathbf{B} = \begin{bmatrix} \frac{\varepsilon' V_o}{2\sqrt{3}} \left(\sin\theta_v - \frac{\cos\theta_v}{\sqrt{3}} \right) \\ \frac{\varepsilon' V_o}{2\sqrt{3}} \left(\frac{\sin\theta_v}{\sqrt{3}} + \cos\theta_v \right) \end{bmatrix} \end{cases} \tag{11}$$

$$\text{Lead error}: \begin{cases} \mathbf{T}^{-1}_{dq/\alpha\beta} \mathbf{A} \mathbf{T}_{dq/\alpha\beta} = \begin{bmatrix} \frac{1+\varepsilon}{2} + \frac{2\sqrt{3}\varepsilon'}{3} \sin\theta_v \cos\theta_v & \frac{\varepsilon'}{2\sqrt{3}} \cos\theta_v{}^2 - \frac{\varepsilon'\sqrt{3}}{2} \sin\theta_v{}^2 \\ \frac{\varepsilon'\sqrt{3}}{2} \cos\theta_v{}^2 - \frac{\varepsilon'}{2\sqrt{3}} \sin\theta_v{}^2 & \frac{1+\varepsilon}{2} - \frac{2\sqrt{3}\varepsilon'}{3} \sin\theta_v \cos\theta_v \end{bmatrix} \\ \mathbf{T}^{-1}_{dq/\alpha\beta} \mathbf{B} = \begin{bmatrix} \frac{\varepsilon' V_o}{2\sqrt{3}} \left(\frac{\cos\theta_v}{\sqrt{3}} - \sin\theta_v \right) \\ \frac{\varepsilon' V_o}{2\sqrt{3}} \left(-\cos\theta_v - \frac{\sin\theta_v}{\sqrt{3}} \right) \end{bmatrix} \end{cases} \tag{12}$$

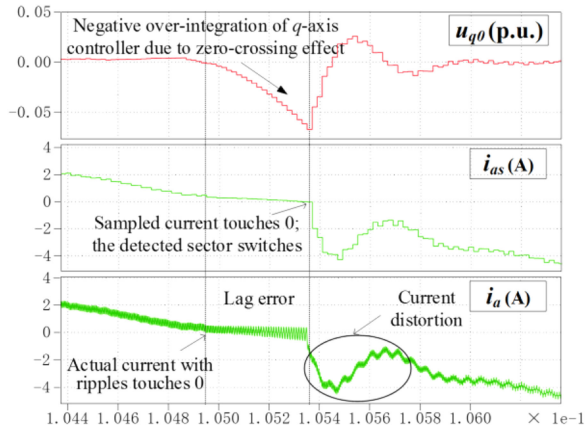

Fig. 9. Detailed waveforms of the zero-crossing effect: (top) q-axis control output; (middle) sampled current in digital controller; and (bottom) actual current.

the zero-crossing effect is equivalent to multiplying the original q-axis control output u_{q0} by ε and adding two interference terms to it.

Usually, the error sector judgment $(\varepsilon < 1)$ is mainly caused by the sampling delay, the current ripple and the phase shifting between leg voltage and inductor current if the sector is decided by the voltage angle. If the sector is decided by the current, the phase shifting can be avoided but the sampling bandwidth and noise suppression must be well designed. Using the voltage angle from phase-locked loop to decide the modulation sectors at unity power factor can avoid the current sampling delay and the noise issue. But some extra calculation must be done with the duty cycle information to avoid the phase shifting.

Fig. 9 shows the q-axis control output, the sampled current in the digital controller and the actual converter-side current near the zero-crossing point. The sampled current is a stepped wave of the actual current with sampling delay. Due to the presence of switching ripple in current, ε gradually decreases from 1 when the average current is close to zero. Before the sampled current crosses zero point, the lag error occurs and the zero-crossing effect will make the equivalent actual output larger than the original output u_{q0}. According to Fig. 4 and expression (6), the actual vector will lead the expected vector when the lag error occurs near zero crossings. In order to maintain the waveform quality, the q-axis closed-loop controller will additionally output a part of negative control quantity, as shown at the top of Fig. 9. This part of negative control quantity offsets the zero-crossing effect caused by the lag error. More specifically, since the closed-loop current controller is introduced, the lead effect of the actual output in the lag error areas will be compensated by the regulation. The q-axis control output will accumulate negatively before the sector switching. Once the sampled current crosses zero points, the converter is affected by the lead error instead of the lag error. Then, the negative accumulation causes a current spike without compensation. The total process is shown in Fig. 9.

If the control output is limited, the high-order distortion peak after the sector switching will be limited partly since the negative control accumulation is not allowed. However, before the sampled current crosses zero points, the compensation output as well as effect are also limited in this case. Hence, zero-crossing effect in the lag error area becomes significant. The low-order distortion will be larger.

As shown in Fig. 8, the zero-crossing effect makes the equivalent q-axis output larger than the original output. Thus, the accumulated negative control quantity with the lead error effect will produce a large current distortion. The current will quickly move away from the zero and produce a large spike until the controller recovers from the oscillation. Since the effect of the lead error and the accumulated negative control output caused by the lag error both keep the current away from zero, the lead error area is extremely small.

IV. Compensation Method for Zero-Crossing Distortion

The sector error will distort the current waveform. The inevitable sector error caused by ripples of the converter-side current is the major problem. Other factors such as the current sampling delay can also lead to the sector error. According to the actual applications, the total sampling delay is generally about one sampling period, and its influence on the components in the control band is negligible. For a properly designed system, the sampling delay has little effect on zero-crossing distortion. However, if a high-order filter such as the *LCL* filter is adopted, the ripples of the converter-side current can be relatively large. In this situation, the current distortion problem at zero-crossing points will be more serious. Fig. 10(a) shows an example of a Vienna rectifier system with zero-crossing distortion. The parameters involved in the simulation system are given in Table II. In Fig. 10(a), a large peak current can be observed at the zero-crossing points.

Section III has proposed the equivalent model considering the zero-crossing effect. Based on the proposed model, two compensation methods are presented as follows to reduce the zero-crossing distortion.

As analyzed and described at the end of Section III, the effect of the lag error can be compensated by the current controller. The main problem is that the negative control accumulation will cause large current distortion after the detected sector switching. If we want to avoid serious zero crossings, the actual equivalent q-axis output u_q should be continuous

$$\begin{cases} u_{q0_{\rm str}} = \frac{\varepsilon_{ch}}{\varepsilon_{ne}} u_{q0_{\rm end}} + \frac{2-\varepsilon_{ch}-\varepsilon_{ne}}{\sqrt{3}\varepsilon_{ne}} \left(\frac{V_o}{\sqrt{3}} - u_d \right) \\ \text{with lead error when sampling} : 0.5 < \varepsilon_{ne} < 1 \\ \text{without lead error when sampling} : \varepsilon_{ne} = 1 \end{cases} \tag{15}$$

where $u_{q0\_\rm end}$ is the q-axis control output of the last period before the sector switching; $u_{q0\_\rm str}$ is the q-axis control output of the first period after the sector switching; u_d is the d-axis control output; ε_{ch} is the sector detection accuracy of the last period before the sector switching; and ε_{ne} is the sector detection accuracy of the next period after the sector switching. In addition, it is worth noting that we should also normalize V_o if the control outputs u_d and u_q are normalized, which happens frequently when we implement the algorithm in the digital controllers.

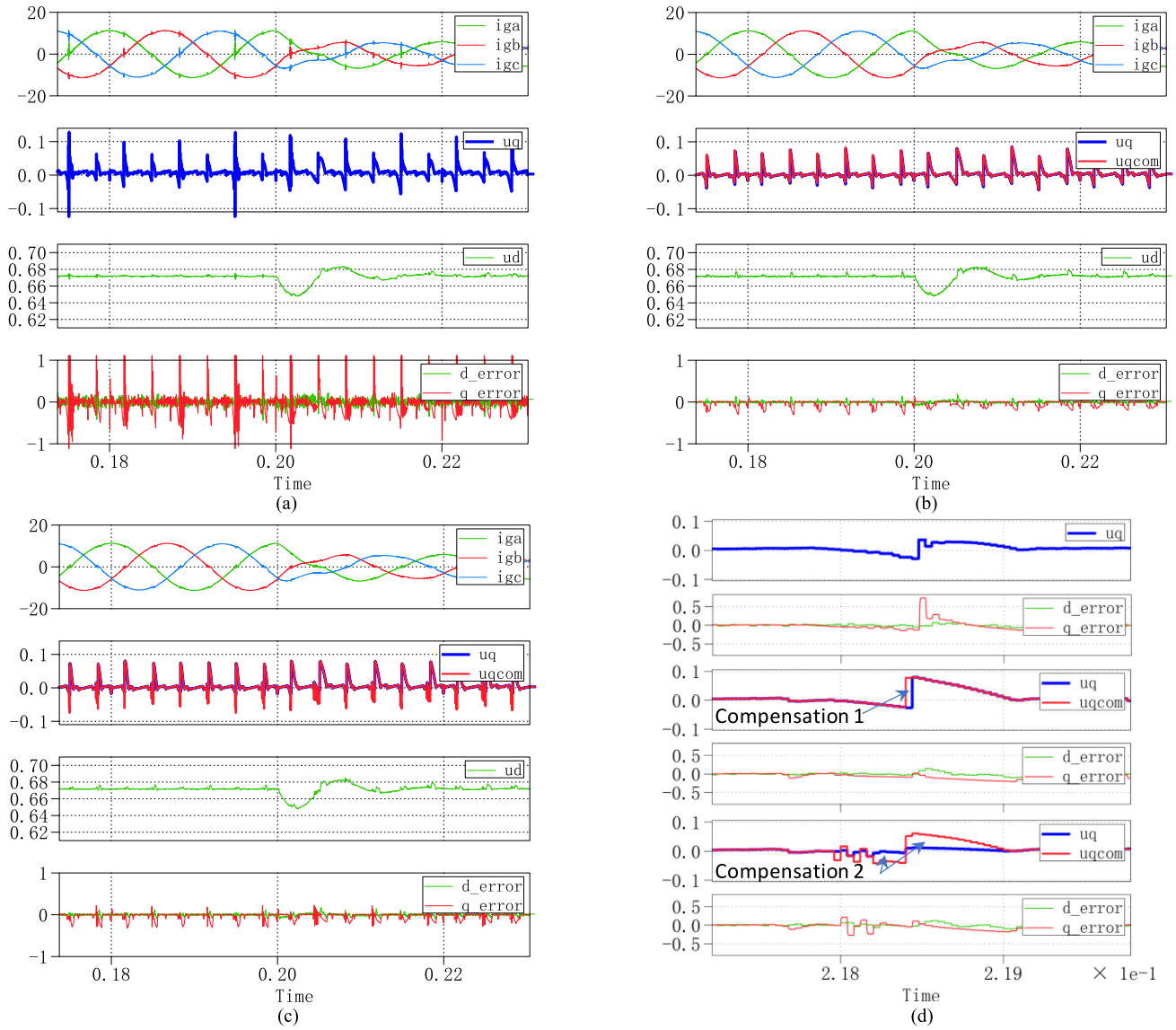

Fig. 10. Grid currents of Vienna rectifier with and without compensation. (a) Without compensation. (b) With compensation (15). (c) With compensation (17) and (19). (d) Detailed view for q-axis control output.

TABLE II
PARAMETERS OF THE SYSTEM

Parameter	Value	Parameter	Value
Grid phase voltage V_g	220 V/50 Hz	DC-bus voltage V_o	750 V
Switching frequency f_s	60 kHz	Sampling frequency (Control frequency) f_c	60 kHz
Converter-side inductor L_s	400 uH	Grid-side inductor L_g	180 uH
Filter capacitor C_f	940 nF	Load resistance R_L	110 Ω
Proportional gain of current controller K_{cp}	0.015	Integral gain of current controller K_{ci}	240
Proportional gain of voltage controller K_{vp}	0.05	Integral gain of voltage controller K_{vi}	63

In this case, the actual equivalent q-axis output will not be abrupt and the large current distortion can be avoided. The zero-crossing effect in the lag and lead error areas (low-band distortions) is compensated by the regulation of the closed-loop controller itself. Usually, ε_{ch} is slightly smaller than 0.5 since the sampling occurs at the midpoint of the switch. When considering the control delay and the controller effect, the lead error may not occur. Due to the control delay, however, ε_{ne} is no longer equal to $1-\varepsilon_{ch}$. Considering the sampling delay, the sampling after sector switching may be in the lead error area (the first condition) or not (the second condition). If the first condition in (15) is used but the second condition occurs (without lead error), the output will overshoot. The controller and the sector detection may oscillate. If the second condition in (15) is used but the first condition occurs (with lead error), the control will undershoot. However, the control undershoot does not cause oscillations and it can be quickly compensated by the controller. Hence, the second compensation condition is recommended for use if the compensation amount is not automatically tuned by feedback. ε_{ch} and ε_{ne} will be influence by many factors, such as the current ripple, the sampling delay and offset deviation.

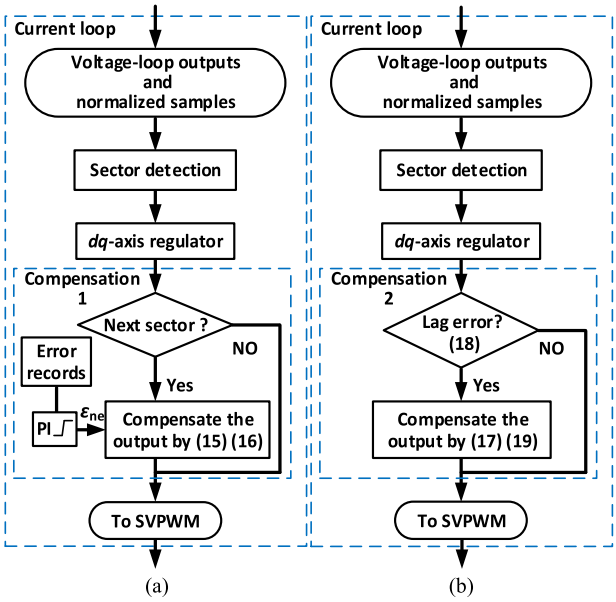

Fig. 11. Flowchart of the current loop with compensation. (a) Compensation (15). (b) Compensation (17)–(19).

The easiest way is to set $\varepsilon_{ch} = 0.5$ and $\varepsilon_{ne} = 1$. In this case, the zero-crossing distortion can be partially eliminated without risks of overcompensation or difficulties in controlling. For better performance, an online closed-loop adjustment process is proposed for ε_{ch} and ε_{ne} for better performance as follows.

The actual equivalent q-axis output u_q in the last period before the sector switching is almost equal to the one without the zero-crossing effect considering the close-loop controller, though the original q-axis control output u_{q0} has changed a lot. In other words, u_{q0} reflects the sector judgment error that is influenced by many factors. By omitting the high frequency difference, the steady state of u_q under unit power factor can be acquired as $\omega L_s i_d V_o / V_{cd}$ based on the model proposed in [12]. It is adopted as the average value to estimate the instantaneous value. Then, according to the equivalent model of zero-crossing effect in Fig. 8, the estimated (steady) value of ε_{ch} is derived as

$$\varepsilon_{ch} = \frac{1 - u_d - \sqrt{3} u_d \omega L_s i_d / V_{cd}}{1 - u_d - \sqrt{3} u_{q0\_\mathrm{end}}} \tag{16}$$

where V_{cd} is the d-axis quantity of the capacitor voltage; and ω is the grid voltage angular frequency.

To resist the interference of the measurement offset, the control delay and so on, a closed loop controller is adopted to calculate ε_{ne}, which is shown in Fig. 11. The aim of the controller is to keep the current difference Δi_{2p} between the first and the second periods after sector switching to the ideal reference $\Delta I_r = I_{dM} \sin(\omega T_c)$, where T_c is the control period. After each same sector switching, the current samples of the first and the second periods are recorded to get Δi_{2p}. Then, the error $\Delta I_r - \Delta i_{2p}$ is acquired as the input of the controller to calculate ε_{ne}. As is analyzed, a larger amount of compensation will cause smaller current change (undershoot) while a small compensation will cause overshoot. A proportional integral controller or just an integral controller can be adopted. Through the closed loop adjustment process, most of the steady interference (the control delay and the measurement offset) will be suppressed and the better performance can be achieved. However, at least two control loops need to be added and calculated. In fact, good but not the best performance can be achieved by setting a fixed value $\varepsilon_{ne} = 1$ and the calculation process can be reduced.

Fig. 10(b) shows the grid currents of the same Vienna rectifier system after introducing the compensation term (15). It shows that the terrible spike current is eliminated near the zero-crossing points, though the slope of the current changes slightly. Thus, there is less current distortion after introducing the compensation method.

The second method is to offset the additional terms by compensating the q-axis control output when the sector error occurs. If the additional control quantity is added to the q-axis control output according to the model in Fig. 8, the zero-crossing distortion can be eliminated. Therefore, the compensated q-axis output u_{q0c} should be

$$u_{q0c} = \frac{u_{q0}}{\varepsilon} - (-1)^{si} \frac{1-\varepsilon}{\sqrt{3}\varepsilon} u_d - (-1)^{si+1} \frac{1-\varepsilon}{3\varepsilon} V_o. \tag{17}$$

When the neutral point N_f of the three-phase filter is connected to the dc neutral point M (this method is often used to improve the dc-side EMC characteristics), the criterion for the existence of zero-crossing effect is

$$\text{If}: \ |I_x| < \left| \frac{T_s d_x U_{xNf}}{2L_s} \right|$$
$$\begin{cases} \text{Before sector switching} => \text{lag error}; \\ \text{After sector switching} => \text{lead error}; \end{cases} \tag{18}$$

where I_x is the converter-side current of the zero-crossing phase; U_{xNf} is the corresponding phase voltage to neutral point N_f; d_x is the duty ratio of the corresponding phase; T_s is the switching period; and L_s is the converter-side inductance. ε is calculated as

$$\varepsilon = \left| \frac{2 I_x L_s}{T_s d_x U_{xNf}} \right|. \tag{19}$$

When the neutral point N_f of the three-phase filter is not connected to the dc neutral point M, the calculation of ε is more complicated since the inductor voltage contains more levels. However, the earlier analysis is a simplification that does not consider the voltage difference between the two neutral points. Because the period value of the voltage difference in steady state is zero and three-phase switch actions are symmetrical, the earlier calculation is still effective. Simulations and experiments can prove that (17)–(19) are effective even without connecting two neutral points, so there is no need for a more accurate but complex calculation of ε. Moreover, as analyzed earlier, the lead error area is small due to the characteristics of the lead error. The compensation for the lead error can be omitted.

Fig. 10(c) shows the grid currents of the same Vienna rectifier system after introducing the compensation terms (17)–(19). In Fig. 10(c), the terrible spike current is eliminated and there is almost no current distortion before the sector switching. Because

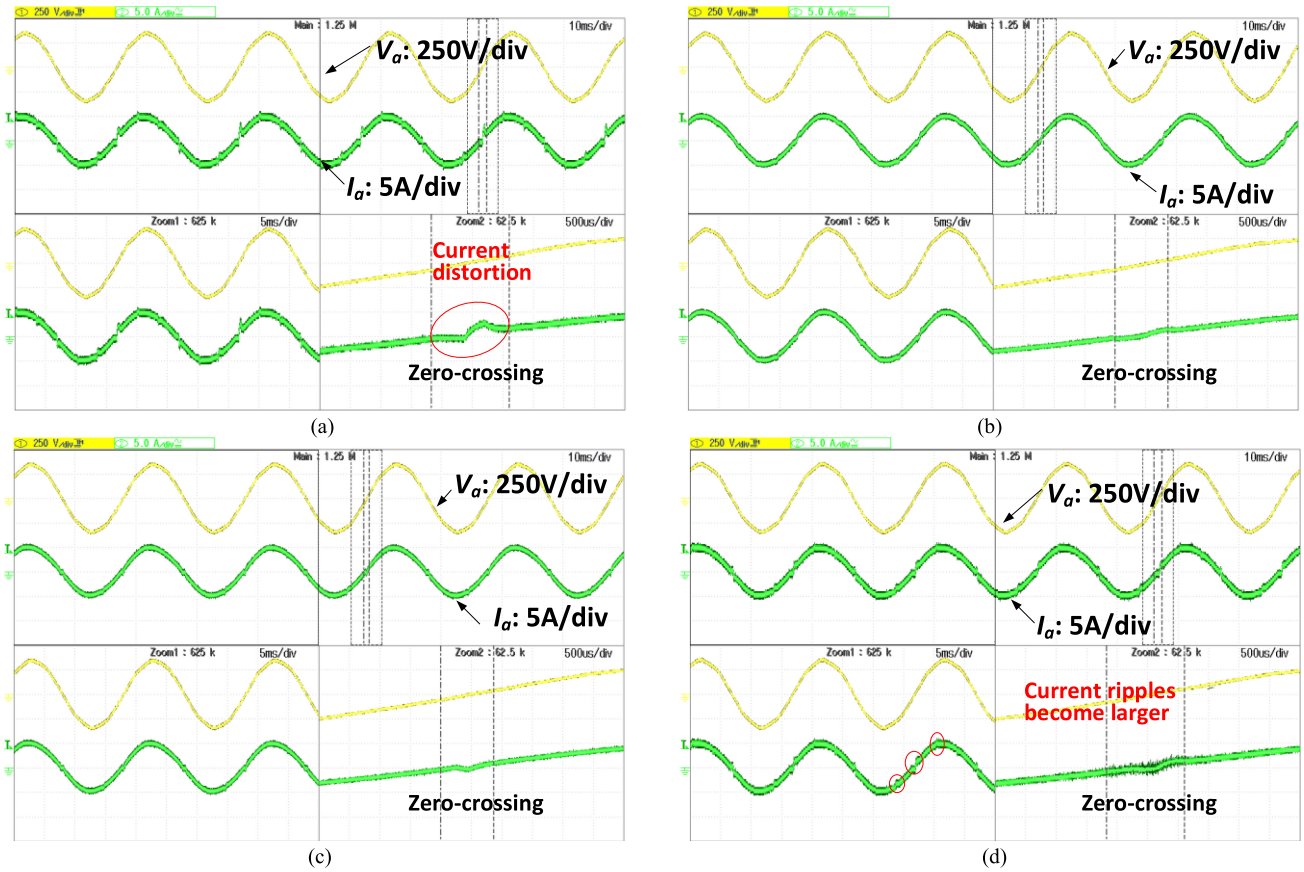

Fig. 12. Key waveforms of the Vienna prototype. (a) Without compensation. (b) With compensation 1. (c) With compensation 2. (d) With compensation in [17].

TABLE III
DIFFERENT PARAMETERS OF THE PROTOTYPE

Parameter	Value
Converter-side inductor L_s	403/412/407 uH
Grid-side inductor L_g	174/182/176 uH
Filter capacitor C_f	938/938/940 nF
Load resistance R_L	240 Ω

the compensation of the lead error is omitted for easy algorithm implementation, the slope of the current changes in a small area after the sector switching. Nevertheless, the quality of the zero-crossing current is sufficiently satisfactory.

These compensation methods can be easily implemented in a digital controller and the flowchart of the current-loop control with compensation is shown in Fig. 11.

V. EXPERIMENTAL RESULTS

The theoretical analysis and the proposed compensation methods are further evaluated by an experimental prototype. The control strategy adopted is already depicted in Fig. 1, and the compensation process shown in Fig. 11 is cooperated to deal with the zero-crossing distortion problem. The constructed experiment is designed with the same parameters as those given in Table II except the power level, the differences are given in Table III. The controller of the prototype is implemented with one Infineon XMC4500 ARM processor, which is a 32-bit floating-point MCU with 120 MHz system clock. The experimental results with an output power of 2.35 kW are given in Fig. 12. The method proposed in [17] is also tested in the experiment for comparison. The zero-crossing area in which the switches are kept "ON" state is decided using the same conditions with the compensation method 2 in Section IV.

Fig. 12(a) shows the key waveforms of the Vienna prototype. The *LCL* filter is used here, so the converter-side current is relatively large though the switching ripples of the grid-side current are small enough. The detailed scope of the input current near the zero-crossing point is also shown in this figure. When the current ripples hit the zero line, the current begins to be distorted. After the sector switching, an overshoot current can be observed. This process is consistent with the proposed model. The total harmonic distortion of the grid-side current (THDi) is 4.85%, is mainly caused by low-order harmonics.

Fig. 12(b) shows the experimental waveforms after adopting the compensation method 1 displayed in the left part of Fig. 11. From the detailed scope of the input current, it can be seen that the waveforms before the zero-crossing points are basically the same with the Fig. 12(a). However, the overshoot current is eliminated since the accumulated negative control quantity is compensated. The THDi in this case is 3.01% and the zero-crossing harmonics (300–5000 Hz) are significantly reduced. If there is no deviation between the ideal compensation amount and

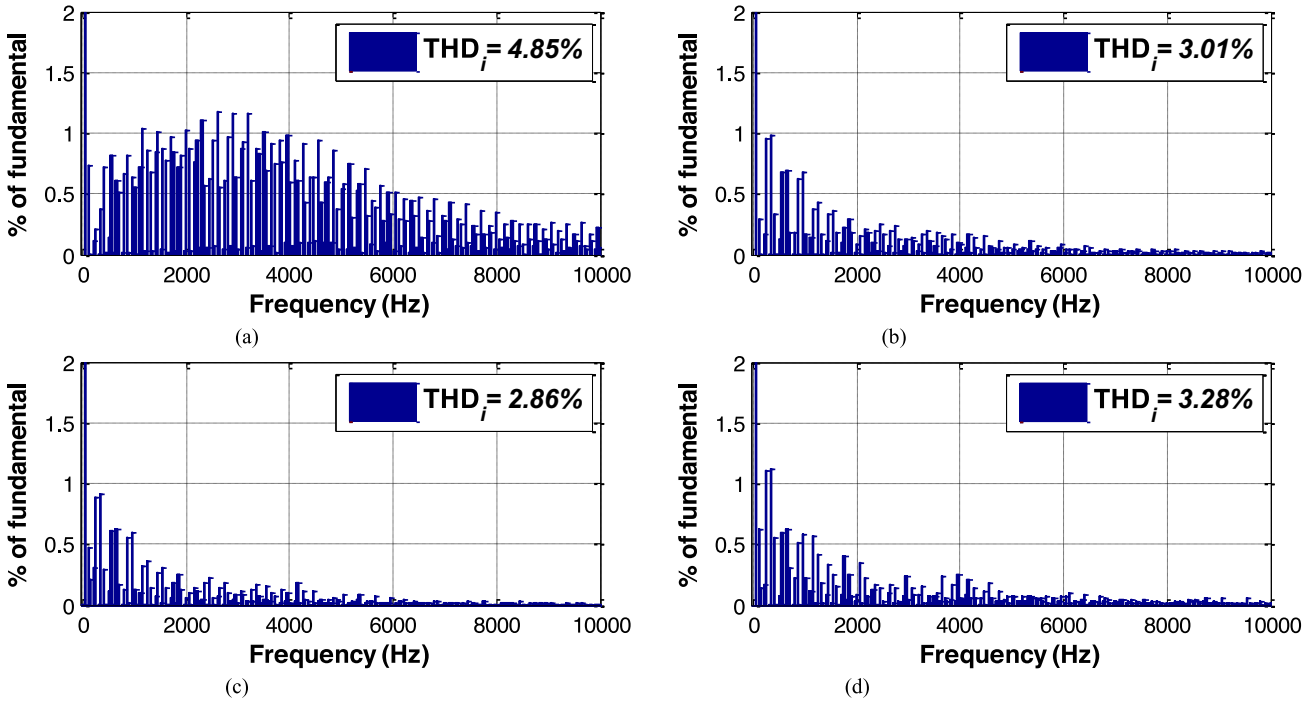

Fig. 13. Fast Fourier transform results of grid-side currents. (a) Without compensation. (b) With compensation 1. (c) With compensation 2. (d) With compensation in [17].

TABLE IV
FLUCTUATIONS OF MIDPOINT VOLTAGE

Scheme	Midpoint voltage fluctuation (peak)
Without compensation	6.1 V (0.81%)
With compensation 1	5.5 V (0.75%)
With compensation 2	5.6 V (0.75%)
With compensation in [17]	8.1 V (1.08%)

the used compensation amount, the high harmonic components are completely eliminated while the low harmonic components will not increase. Unfortunately, there is always the existence of small deviation and the low harmonic components may slightly increase. However, the compensation is still effective and the THD*i* is drastically reduced.

Fig. 12(c) shows the experimental waveforms after adopting the compensation method 2 displayed in the right part of Fig. 11. The quality of the current waveform near the zero-crossing points have been further improved in this experiment. Though some tiny low-order harmonics (100–300 Hz) are introduced since the leg voltage is used in this compensation method, the zero-crossing distortion is completely eliminated and the THD*i* is reduced. The THD*i* in this case is reduced to 2.86%.

Fig. 12(d) shows the experimental waveforms after adopting the compensation method proposed in [17]. The zero-crossing distortion is eliminated since the switching states which may lead to the step of duty ratios are gives up. However, the current ripples become larger once the compensation is adopted. The THD*i* in this case is about to 3.28%. In fact, the five-segment modulation is used at this time. The fluctuation of the midpoint voltage is also slightly larger since the switching control of one phase is lost and the small vectors are limited. However, the two proposed methods are still maintained as seven-segment modulation. Table IV shows the fluctuations of the midpoint voltage.

Fig. 13 shows the frequency spectrums of the grid-side currents for the four experiments. In the conventional method, the low-order harmonics, especially the $(6k \pm 1)$ order harmonics, have the magnitude larger than those with the compensation methods due to the zero-crossing effect. It shows that the proposed model reasonably describes the effect of zero-crossing effect on current distortion. However, when the proposed methods are adopted, the current distortion caused by zero-crossing effect is significantly reduced. It can be concluded that the proposed control scheme has good performance in zero-crossing distortion elimination.

Moreover, the proposed methods are easier to implement in practical applications than almost all other methods and will not influence the original program. For example, the method in [17] should modify the modulation method (so affects action qualifier (AQ) register in digital signal processor (DSP) or the equivalent) when implementing.

VI. CONCLUSION

This article has researched the zero-crossing current distortion problem and presented an equivalent model considering the zero-crossing effect for Vienna rectifiers. The nonshared switching states and the nonshared vectors, which lead to the current distortion when the sector detection error occurs, are explained and listed in detail. The sector detection errors can be divided into two types: the lag error and the lead error.

Different detection errors will produce different zero-crossing effects. Moreover, the equivalent control block considering the zero-crossing effect is modeled. We can quantitatively find the effect of sector detection errors on the control output through the proposed model. From mathematical derivation as well as numerical simulation, it can be found through the model that the zero-crossing current distortion is mainly affected by the current ripple, the phase delay, the controller (control type and bandwidth), the grid-side voltage level and harmonics. For Vienna converters using small converter-side inductance (*LCL*/*LLCL*) and high bandwidth current controller, the zero-crossing distortion problem is more obvious. The article mainly analyzes and solves this problem. The main contributions are summarized as follows.

1) The paper defines and analyzes the nonshared switching states and the corresponding nonshared vectors. The effect of nonshared vectors is detailed in the lag/lead error area.
2) Based on 1), the equivalent *dq*-frame zero-crossing effect model is proposed. This model mathematically depicts the zero-crossing effect as additional coupled interference terms in the system loop.
3) Based on 2), two compensation methods for zero-crossing effect are proposed without increasing the control complexity. The proposed methods significantly reduce the current distortion at zero-crossing points and can be adopted in practical applications for both traditional SVPWM and equivalent CBPWM techniques easily.

The proposed model and control schemes were verified in simulations and experiments. As a general solution to the zero-crossing current distortion problem for Vienna rectifiers, the proposed methods can be readily applied in practical applications.

REFERENCES

[1] X. Li, Y. Sun, H. Wang, M. Su, and S. Huang, "A hybrid control scheme for three-phase Vienna rectifiers," *IEEE Trans. Power Electron.*, vol. 33, no. 1, pp. 629–640, Jan. 2018.

[2] Q. Wang, X. Zhang, R. Burgos, D. Boroyevich, A. M. White, and M. Kheraluwala, "Design and implementation of a two-channel interleaved Vienna-type rectifier with >99% efficiency," *IEEE Trans. Power Electron.*, vol. 33, no. 1, pp. 226–239, Jan. 2018.

[3] S. Prakash P, R. Kalpana, B. Singh and G. Bhuvaneswari, "Design and implementation of sensorless voltage control of front-end rectifier for power quality improvement in telecom system," *IEEE Trans. Ind. Appl.*, vol. 54, no. 3, pp. 2438–2448, May/Jun. 2018.

[4] M. S. Ortmann, S. A. Mussa, and M. L. Heldwein, "Three-phase multilevel PFC rectifier based on multistate switching cells," *IEEE Trans. Power Electron.*, vol. 30, no. 4, pp. 1843–1854, Apr. 2015.

[5] J. Lee and K. Lee, "Predictive control of Vienna rectifiers for PMSG systems," *IEEE Trans. Ind. Electron.*, vol. 64, no. 4, pp. 2580–2591, Apr. 2017.

[6] L. Hang, B. Li, M. Zhang, Y. Wang, and L. M. Tolbert, "Equivalence of SVM and carrier-based PWM in three-phase/wire/level Vienna rectifier and capability of unbalanced-load control," *IEEE Trans. Ind. Electron.*, vol. 61, no. 1, pp. 20–28, Mar. 2014.

[7] R. Burgos, R. Lai, Y. Pei, F. Wang, D. Boroyevich, and J. Pou, "Space vector modulator for VIENNA-type rectifiers based on the equivalence between two- and three-level converters: A carrier-based implementation," *IEEE Trans. Power Electron.*, vol. 23, no. 4, pp. 1888–1898, Jul. 2008.

[8] J. Lee and K. Lee, "A novel carrier-based PWM method for Vienna rectifier with a variable power factor," *IEEE Trans. Ind. Electron.*, vol. 63, no. 1, pp. 3–12, Jul. 2016.

[9] L. Hang, H. Zhang, S. Liu, X. Xie, C. Zhao, and S. Liu, "A novel control strategy based on natural frame for VIENNA-type rectifier under light unbalanced-grid conditions," *IEEE Trans. Ind. Electron.*, vol. 62, no. 3, pp. 1353–1362, Mar. 2015.

[10] J. Lee and K. Lee, "Carrier-based discontinuous PWM method for Vienna rectifiers," *IEEE Trans. Power Electron.*, vol. 30, no. 6, pp. 2896–2900, Jun. 2015.

[11] J. Lee and K. Lee, "Performance analysis of carrier-based discontinuous PWM method for Vienna rectifiers with neutral-point voltage balance," *IEEE Trans. Power Electron.*, vol. 31, no. 6, pp. 4075–4084, Jun. 2016.

[12] R. Lai, F. Wang, R. Burgos, D. Boroyevich, D. Jiang, and D. Zhang, "Average modeling and control design for VIENNA-type rectifiers considering the Dc-Link voltage balance," *IEEE Trans. Power Electron.*, vol. 24, no. 11, pp. 2509–2522, Nov. 2009.

[13] J. W. Kolar and T. Friedli, "The essence of three-phase PFC rectifier systems—Part I," *IEEE Trans. Power Electron.*, vol. 28, no. 1, pp. 176–198, Jan. 2013.

[14] J. Adhikari, P. IV, and S. K. Panda, "Reduction of input current harmonic distortions and balancing of output voltages of the Vienna rectifier under supply voltage disturbances," *IEEE Trans. Power Electron.*, vol. 32, no. 7, pp. 5802–5812, Jul. 2017.

[15] B. Liu, R. Ren, E. A. Jones, F. Wang, D. Costinett, and Z. Zhang, "A modulation compensation scheme to reduce input current distortion in GaN-based high switching frequency three-phase three-level Vienna-Type rectifiers," *IEEE Trans. Power Electron.*, vol. 33, no. 1, pp. 283–298, Jan. 2018.

[16] M. Hartmann, H. Ertl, and J. W. Kolar, "Current control of three-phase rectifier systems using three independent current controllers," *IEEE Trans. Power Electron.*, vol. 28, no. 8, pp. 3988–4000, Aug. 2013.

[17] W. Yao, Z. Lv, M. Zhang, and Z. Lin, "A novel SVPWM scheme for Vienna rectifier without current distortion at current zero-crossing point," in *Proc. Int. Symp. Ind. Electron.*, 2014, pp. 2349–2353.

[18] H. Xu, W. Yao, and S. Shao, "Improved SVPWM schemes for Vienna rectifiers without current distortion," in *Proc. IEEE Energy Convers. Congr. Expo.*, 2017, pp. 3410–3414.

[19] T. Friedli, M. Hartmann, and J. W. Kolar, "The essence of three-phase PFC rectifier systems—Part II," *IEEE Trans. Power Electron.*, vol. 29, no. 2, pp. 543–560, Feb. 2014.

[20] W. Ding, C. Zhang, F. Gao, B. Duan, and H. Qiu, "A Zero-Sequence component injection modulation method with compensation for current harmonic mitigation of a Vienna rectifier," *IEEE Trans. Power Electron.*, vol. 34, no. 1, pp. 801–814, Jan. 2019.

[21] L. Dalessandro, S. D. Round, U. Drofenik, and J. W. Kolar, "Discontinuous space-vector modulation for three-level PWM rectifiers," *IEEE Trans. Power Electron.*, vol. 23, no. 2, pp. 530–542, Mar. 2008.

[22] Q. Liu, Y. Li, L. Luo, Y. Peng, and Y. Cao, "Power quality management of PV power plant with transformer integrated filtering method," *IEEE Trans. Power Del.*, vol. 34, no. 3, pp. 941–949, Jun. 2019.

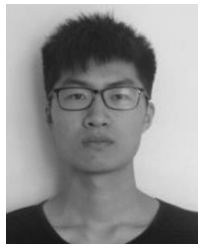

Zheyu Miao (S'19) was born in Hangzhou, Zhejiang Province, China, in 1994. He received the B.S. degree in electrical engineering from Xi'an Jiaotong University, Xi'an, China, in 2016. He is currently working toward the Ph.D. degree with the Department of Electrical Engineering, National Key Laboratory of Power Electronics, Zhejiang University, Hangzhou, China.

His current research interests include the *LLC* resonant converter and digital control technique of power converters.

Hao Tong was born in China in 1996. He received the B.S. degree in electrical engineering from Xi'an Jiaotong University, Xi'an, China, in 2018. He is currently working toward the M.S. degree in power electronics with the Department of Electrical Engineering, National Key Laboratory of Power Electronics, Zhejiang University, Hangzhou, China.

His research interests include modeling and digital control of power conversion circuits including power factor correction converters and Vienna Rectifier.

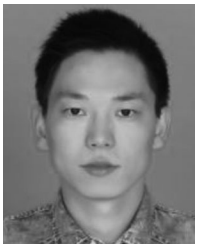

Xiaoguang Jin was born in Hebei, China, in 1983. He received the M.S. degree in electrical engineering from Zhejiang University, Hangzhou, China, where he is currently working toward the Ph.D. degree in electrical engineering.

From 2004 to 2008, he was a Power Supply Designing Engineer with Delta Electronics, China. From 2011 to 2012, he was an Electrical Engineer with One-Cycle Control Inc., Irvine, CA, USA. His research interests include topology and control of power converters for data-center and server power supplies, resonant converters with wide voltage range and battery management systems.

Wenxi Yao (M'12) was born in Haining, Zhejiang Province, China, in 1977. He received the B.S. and Ph.D. degrees in electrical engineering from Zhejiang University, Hangzhou, China, in 2000 and 2006, respectively.

He is currently an Associate Professor in electrical engineering with Zhejiang University. From 2010 to 2011, he was a Visiting Scholar with FREEDM, North Carolina State University, Raleigh, NC, USA. He has authored or coauthored more than 50 published technical papers. His research interests include digital control in power electrics and sensorless control of ac motor drives.

Zhengyu Lu (SM'02) received the B.S. degree in industrial automatic control from Hohai University, Nanjing, China, in 1982, and the Ph.D. degree in power electronics from Zhejiang University, Hangzhou, China, in 1987.

From 1996 to 1998, he was a Visiting Scholar and a Researcher with the University of Birmingham, Birmingham, U.K., and Imperial College, London, U.K. He is currently a Professor with Zhejiang University, and the Director of the China National Power Electronics Laboratory. Since 1982, he has been teaching and conducting research work on power electronic devices and power converters with Zhejiang University. He has authored or coauthored more than 300 papers and has a dozen Chinese patents authorized. His research interests include power converters, electrical tracks, vehicle electronics, electronics in flexible ac transmission system applications, and power electronics system integration.

Zhen Ma was born in Pingdingshan, Henan Province, China, in 1981. He received the M.S. degree in chemical engineering from the East China University of Science and Technology, Shanghai, China in 2006.

He is currently engaged in project management related to switching-mode power supply. His research interests include dc/dc converters and switching-mode power supplies.